A stability study of transparent conducting $WO_3/Cu/WO_3$ coatings with antimicrobial properties

M. Zubkins [a,*], V. Vibornijs [a], E. Strods [a], I. Aulika [a], A. Zajakina [b], A. Sarakovskis [a], K. Kundzins [a], K. Korotkaja [b], Z. Rudevica [b], E. Letko [a], J. Purans [a]

[a] *Institute of Solid State Physics (ISSP), University of Latvia, Kengaraga 8, Riga LV-1063, Latvia*
[b] *Latvian Biomedical Research and Study Centre (LBMC), Ratsupites 1, Riga LV-1067, Latvia*

ARTICLE INFO

ABSTRACT

$WO_3/Cu/WO_3$ coatings are transparent electrodes, but conductivity and transmittance have been observed to decrease with time. This paper reports the improved stability of $WO_3/Cu/WO_3$ coatings deposited by magnetron sputtering on glass and polyethylene terephthalate substrates. The stability issues due to Cu oxidation and migration can be addressed by adjusting the deposition parameters. Lowering the sputtering pressure results in denser WO_3 films, confirmed by spectroscopic ellipsometry, and thus more stable coatings. The coatings retain their properties in an inert atmosphere, indicating that Cu oxidation is the main reason for the decrease in conductivity, rather than its migration observed by X-ray photoelectron spectroscopy. Optical property modeling is used to optimize the thickness of the three-layer coatings to obtain the highest figure-of-merit for a transparent electrode. A structure of glass/WO_3 (70 nm)/Cu (10 nm)/WO_3 (45 nm) gives a sheet resistance of 14 Ω/sq. and a light transmittance of 65% at 600 nm. In addition, the antimicrobial properties of these coatings are revealed. A decrease up to 10^5 of the gram-negative *Escherichia coli* and gram-positive *Staphylococcus aureus* bacterial colony formation units is found for several $WO_3/Cu/WO_3$-based coatings. In the case of the MS2 (*Emesvirus zinderi*) bacteriophage, a decrease in infectious particles for up to 10^4 plaque-forming units is obtained. The results indicate that more stable samples also had higher antimicrobial activity.

1. Introduction

Dielectric-metal-dielectric (DMD) coatings have been demonstrated as possible transparent electrodes in flexible optoelectronic devices [1] to replace the most commonly used indium tin oxide (ITO), which is brittle, requires high production temperatures to achieve high conductivity and has a supply risk due to the natural scarcity of In [2]. To improve the flexibility of the single-layer ITO electrode, the thickness must be very small, which compromises the electrical conductivity. DMD coatings have high conductivity and transparency, excellent flexibility, simple fabrication and good compatibility with various substrates, including polyethylene terephthalate (PET) [1]. In DMD structures, a thin metallic film is sandwiched between two dielectric films to promote high transparency and to protect the metallic film from degradation. The conductivity of these coatings is mainly controlled by the conductivity of the metal film. The ductility of the metal film improves the robustness under mechanical stress and allows the deposition

of thinner electrodes than single-layer electrodes [3]. The figure-of-merit by Haacke [4] for DMD coatings can reach a value of $\sim 10^{-2}$ Ω^{-1}. Although PET/DMD structures can be more stable than PET/ITO, degradation of the DMD itself due to the agglomeration and oxidation of metal atoms is a problem that is still under investigation [5, 6].

There has been a tremendous increase in interest and research into antimicrobial coatings (AMCs) due to the COVID-19 pandemic [7]. Contaminated high-touch surfaces in healthcare or other public areas are an extra source of bacteria and other microorganisms and play an important role in the chain of transmission [8]. In many cases, these pathogens can survive on surfaces for a sufficiently long time to accumulate and cause a variety of serious infectious diseases, thereby threatening human health and creating a heavy economic burden. Although cleaning and disinfecting surfaces can be effective methods to prevent this, they are time-consuming and their effect is only temporary [9]. Another method is the use of self-disinfecting surfaces or so-called

AMCs. Several mechanisms with different functional principles are known to cause surface antimicrobial activity: (i) biocide release, (ii) active contact, (iii) anti-adhesive (superhydrophobic), and (iv) repulsion [10,11]. In principle, these effects can be combined to increase efficiency. Inorganic antibacterial agents, such as Cu, Ag, TiO_2, ZnO and WO_3, are more stable than organic compounds under various adverse conditions. However, the toxicity level of these materials, especially metals in the form of nanoparticles, is still being investigated [12,13]. Referring to a literature survey published in 2019 [14], silver-based AMCs relying on the biocide release mechanism are the most used and studied.

The antimicrobial properties of metal oxides depend on their photocatalytic activity. Under proper light irradiation, reactive oxide species can be produced that can cause damage to microorganisms. Tungsten oxide (WO_3) is a well-known material due to its photocatalytic activity. In addition, WO_3 nanoparticles have been shown to be biologically safe [15]. A relatively narrow band gap of 2.6 eV in the crystalline phase, together with a deep valance band edge, makes it possible to use WO_3 in visible-light-driven photocatalysis. However, WO_3 alone shows low photocatalytic activity because its conduction band is not sufficient to reduce oxygen [16]. To overcome this issue, different interface designs, co-catalysts, sub-stoichiometric compositions and nanostructuring have been employed to increase the photocatalytic efficiency of WO_3. Metal-WO_3 (e.g., Pt-loaded WO_3) and semiconductor-WO_3 (e.g., $WS_2/WO_3 \cdot H_2O$) interfaces can greatly suppress electron-hole recombination [17,18]. Intercalated Cu^{2+} ions have been shown to be promising co-catalysts based on a multi-electron oxygen reduction mechanism [19–21].

The growing applications of AMCs have led to interest in multifunctional coatings that can provide other useful properties, such as visible light transparency and electrical conductivity, in addition to antimicrobial activity. For example, visible-light transparency is crucial for touch panels and solar controlled glasses [22]. $WO_3/M/WO_3$ electrodes have been studied previously [23,24] because they can be deposited by thermal evaporation, which does not degrade organic materials in transparent OLEDs.

In this study, after optimizing and stabilizing the electrical and optical properties of $WO_3/Cu/WO_3$ coatings, we show that they also exhibit antimicrobial properties. More precisely, we show how the deposition pressure, layer thickness and storage conditions influence the properties and stability of the coatings. We demonstrate that the coatings are active against gram-negative and gram-positive bacterial species, *E. coli* and *S. aureus*, respectively, as well as the positive-sense single-stranded enveloped RNA virus MS2 (*Emesvirus zinderi*). The coatings are deposited by direct current magnetron sputtering. Magnetron sputtering is a vacuum plasma technology and among the most widely used types of deposition by the glazing industry because it can be scaled up to large-area substrates together with a high growth rate, which is highly important for large-scale production. These coatings can be synthesized at room temperature, thereby enabling their deposition on flexible substrates and roll-to-roll production.

2. Experimental details

2.1. $WO_3/Cu/WO_3$ deposition conditions

$WO_3/Cu/WO_3$ coatings on soda-lime glass and PET substrates were deposited by DC magnetron sputtering from W (purity 99.95%) and Cu (purity 99.99%) targets. Two ION'X® planar balanced magnetrons (Thin Film Consulting) with target dimensions of $200 \times 100 \times 9$ mm were used. Both magnetrons were placed symmetrically against the substrate holder at a distance of 20 cm. The substrates were cleaned using an ultrasonification bath in acetone and 2-isopropanol sequentially for 15 min each and then drying under blown N_2 gas. The thin film deposition was performed using a vacuum PVD coater G500M.1 (Sidrabe Vacuum, Ltd.). Before the deposition process, the chamber

($\sim$0.1 m^3) was pumped down to a base pressure below 1.3×10^{-5} mbar by a turbo-molecular pump backed with a rotary pump.

The three-layer $WO_3/Cu/WO_3$ coatings were obtained in three consecutive deposition processes. WO_3 films were deposited by sputtering the W target with a power of 300 W in an Ar (99.9999%) and O_2 (99.999%) atmosphere. The depositions were performed at different sputtering pressures from 0.67 to 4.00 Pa and different O_2 to Ar gas flow ratios of 1/2, 2/3, and 5/6 to study the influence on the physical properties of the coatings. A ratio of 2/3 provides the stoichiometric WO_3 films as shown in the previous study [25]. The pumping speed was altered by a throttle valve to set the necessary sputtering pressure. Cu films were deposited by sputtering the Cu target with a power of 300 W at a total pressure of 0.67 Pa in an Ar (30 sccm) atmosphere. Cu films with different thicknesses from 10 to 35 nm were deposited between WO_3 films. Higher Cu thickness significantly decreases visible light transmittance; lower thickness leads to low electrical conductivity due to film discontinuity. The most promising samples were synthesized several times to verify the antimicrobial activity and reproducibility. All characterizations of the physical properties were performed on the samples on glass substrates except for the antimicrobial activity tests. These were carried out on the coatings on PET because a larger number of samples, obtained by cutting a larger piece of PET into smaller ones, is required for high accuracy.

2.2. Characterization of physical properties

The growth rate of WO_3 and Cu under all growth conditions was determined with a profilometer (CART Veeco Dektak 150) by measuring the thickness of the test samples. The deposition time of each film was adjusted accordingly to obtain the planned (hereinafter nominal) layer thickness of the $WO_3/Cu/WO_3$ coatings (Table 1). For the first set of samples, the WO_3 thicknesses were refined after spectroscopic ellipsometry (SE) analysis of the single-layer WO_3 (bottom) films.

The electrical properties of the coatings were measured differently for the two types of sample geometries. To measure the sheet resistance of the inner Cu film ($R_{S,Cu}$) with a simple multimeter, the coatings were deposited on previously prepared glass substrates (25×50 mm) with electrical contacts (Cu 100 nm) on the sides so that the Cu film was in contact with them (first set of samples in Table 1). The geometry of these

Table 1

Deposition parameters and thicknesses of three-layer $WO_3/Cu/WO_3$ coatings. The deposition pressure and O_2 flow rate during growth are the same for both WO_3 (bottom and top) films. The nominal thicknesses are rounded to the nearest five. The thickness structure obtained from the SE modeling of three-layer coatings is also presented.

Sample	WO_3 deposition p (Pa)	O_2 flow rate during WO_3 deposition (sccm)	Nominal WO_3/ Cu/WO_3 thicknesses (nm)	$WO_3/Cu/WO_3$ thicknesses obtained from SE (nm)
First set of samples				
1	0.67	20	95/20/95	94/15/98
2	1.00	20	75/20/75	67/24/87
3	1.35	15	90/20/90	73/40/99
4	1.35	20	50/20/50	50/22/51
5	1.35	20	85/20/85	–
6	1.35	20	90/20/90	83/24/95
7	1.35	20	95/20/95	–
8	1.35	20	115/20/115	124/20/112
9	1.35	20	90/35/90	99/34/87
10	1.35	20	115/50/115	86/52/113
11	1.35	25	90/20/90	79/25/110
12	2.00	20	85/20/85	72/34/89
Second set of samples				
13	0.67	20	25/10/35	–
14	0.67	20	25/15/35	–
15	0.67	20	25/15/50	–
16	0.67	20	70/15/45	–
17	4.00	20	20/15/35	–

samples can be seen in Fig. S1(a). It was a three-step process: (a) deposition of Cu contacts, (b) deposition of first WO$_3$ film, and (c) deposition of the rest of the coating, that is, Cu/WO$_3$. After each step, the chamber was opened to readjust the deposition masks in front of the substrate. After the second step, the single-layer WO$_3$ samples were measured and analyzed by SE.

The second type of samples were deposited on 10 × 10 mm glass substrates (Fig. S1(b)) and the sheet resistance of the three-layer surface ($R_{S,WCW}$) was measured in the van der Pauw configuration using an HMS-5000 system, Ecopia. In this case, all three films were deposited in consecutive deposition runs without venting the chamber (second set of samples in Table 1). After the samples were removed from the chamber, four small ohmic contacts at the corners of the samples were made of high-purity silver paint (SPI-PAINT).

X-ray photoelectron spectroscopy (XPS) was used to study the chemical composition of the samples. The XPS measurements were carried out using a ThermoFisher ESCALAB Xi+ instrument using a monochromatic Al Kα X-ray source. The calibration of the binding energy scale was confirmed by examining sputter-cleaned Au, Ag and Cu reference samples that place Au 4f$_{7/2}$, Ag 3d$_{5/2}$ and Cu 2p$_{3/2}$ peaks at 83.96, 368.21 and 932.62 eV, respectively. The charge neutralization by flow of low energy electrons was used in the reported experiments. The spectra were recorded using an X-ray beam size of 650 × 100 μm with a pass energy of 20 eV and a step size of 0.1 eV. Data from all materials were referenced using the main signal of the carbon 1s spectrum assigned to occur at 284.8 eV. The carbon 1s spectrum was collected using high-energy-resolution settings. A monatomic Ar$^+$ ion gun (energy of 2 keV) was used to study the depth distribution of W, O and Cu.

The structure of the samples was examined by an X-ray diffractometer with Cu-Kα radiation (Rigaku MiniFlex 600). The film surfaces were characterized by scanning electron microscopy (SEM) and the lamella were prepared using a focused ion beam (FIB). Before lamella preparation on the sample surface, a 30 nm thick Au layer was sputtered and a 300 nm thick Pt layer was deposited above to protect the surface from FIB exposure. The lamella cross sections were visualized by both SEM (Thermo Scientific Helios 5 UX dual-beam) and transmission electron microscopy ([TEM], Fei Tecnai G2 F20).

The transmittance and reflectance of the coating, in the range of 250 to 2000 nm, were determined by a spectrophotometer (Agilent Cary 7000). The sample was placed at an angle of 6° against the incident beam and the detector was placed at 180° behind the sample to measure transmittance and at 12° in front of the sample to measure specular reflectance.

The optical properties and layer thicknesses were obtained by employing a WOOLLAM RC2 ellipsometer in a range from 210 to 1690 nm (5.9 to 0.7 eV). The main ellipsometric angles Ψ and Δ were measured at the incident angles from 55° to 70° with a 5° step. The evolution of the Ψ and Δ spectra was studied together with in-depth SE modeling only for the first set of samples (Table 1). Refractive index *n* and extinction coefficient *k* dispersion curves were modeled using Gaussian and Tauc-Lorentz oscillator (TLO) functions [26]. The surface roughness was modeled utilizing the Bruggeman effective medium approximation (EMA) [27]. The optical gradient of (*n; k*) was calculated by dividing the film layer into sub-layers with smaller thicknesses to vary the (*n; k*) dispersion curves from the bottom to the top of the film [28] and by applying the EMA, considering the films as a mixture of (i) WO$_3$ and voids or (ii) WO$_3$, voids, and CuO for both WO$_3$, and (iii) WO$_3$ and Cu for the middle Cu film. Fig. S2 schematically illustrates the ideal and non-ideal three-layer systems considering the EMA and depth profile described above. SE experimental data model-based regression analyses were performed with the WOOLLAM software CompleteEASE®. The substrate and films were modelled as isotropic materials.

2.3. Antimicrobial testing

The anti-bacterial testing methodology was based on the JIS Z 2801

"Antimicrobial products-Test for antimicrobial activity and efficacy" testing standard. Identical testing steps were performed for the *E. coli* ATCC 25,922 and *S. aureus* ATCC 25,923 bacterial cultures received from the microorganism culture collection of the Latvian Biomedical Research and Study Centre (LBMC). Testing samples with dimensions of 15 × 15 mm and thin PET film pieces with dimensions of 10 × 10 mm were prepared following immersion in 96% ethanol, dried out and held in a sterile environment before bacterial culture application. Bacterial suspensions of 1 × 10^7 colony-forming units (CFU)/mL were prepared in a liquid Luria-Bertani (LB) broth with 12 h of growth at 37°C and shaking at 220 rpm using the standard optical density calibration method. A 50 μL bacterial suspension was applied on testing surfaces and covered with a PET film. After 2 h of incubation at room temperature (RT), the testing surface was washed by adding 1 mL of LB broth and the re-suspended bacteria were plated on LB agar plates. After incubation, colonies on agar were counted and A=N/C×V equation was applied, where *A* - CFU/ml, *N* - colonies quantity on plate, *C* - plated decimal dilution, and *V* - plated suspension volume. To measure the log reduction rate caused by samples application, CFU/mL after contact with samples were subtracted from CFU/mL after contact with control PET substrate.

The MS2 (*Emesvirus zinderi*) bacteriophage and *E. coli* XL1-Blue target cell cultures for infection were also received from the microorganism culture collection of LBMC. To evaluate the antiviral properties of the test samples, a 50 μL MS2 suspension with a concentration of 10^8 plaque-forming units (PFU)/mL was added to the test surface, covered with PET and incubated for 2 h at RT. After incubation, the samples were washed from the surface with LB broth and decimal dilutions were prepared and plated using a double-layer agar method with *E. coli* XL1-Blue for standard plague count evaluation. PFU/mL counting and calculation is similar to CFU/mL data acquisition.

All samples were tested at least three times and the log reduction calculations were represented as mean values.

3. Results and discussion

3.1. Sheet resistance and its stability

The deposited WO$_3$/Cu/WO$_3$ coatings were partly transparent in the visible-light range with good adhesion to soda-lime glass substrates. The surface conductivity of the first set of samples (Table 1) was extremely low or in most cases unmeasurable. This was caused by several factors. It was discovered later that the thicknesses (≥50 nm) and sputtering pressures (≥1 Pa) of both WO$_3$ films were not favorable for achieving stable conductivity, as discussed in more detail below. However, we were able to measure the sheet resistance of the inner Cu film ($R_{S,Cu}$) for the samples produced in the geometry shown in Fig. S1(a). The $R_{S,Cu}$ measured immediately after deposition ranged from ~10 to ~40 Ω/sq. depending on the deposition parameters and the thickness of the samples. In one case, the resistivity of the inner Cu film was monitored during the growth of the upper WO$_3$ film to check for possible oxidation due to the reactive deposition process of WO$_3$; however, no change in resistance was observed, meaning that the possibility of strong Cu oxidation can be dismissed. In contrast, the $R_{S,Cu}$ increased over a longer period of time after exposure to air, as can be seen in Fig. 1.

The instability of WO$_3$/Cu/WO$_3$ coatings produced by thermal evaporation has been reported previously and explained by Cu migrating into the WO$_3$ layers [29]. Cu can diffuse through the entire upper WO$_3$ film and accumulate on the surface at up to 10–20 at.% [30]. It has been shown that the diffusion of Cu can be prevented by alloying it with Ni, Al or Ag [30,31], or reduced by introducing a diffusion barrier [32]. When Cu diffusion is suppressed, not only is the conductivity stabilized but higher visible-light transmittance can also be achieved. In our case, we could stabilize the coatings by adjusting the deposition parameters, for example, reducing the deposition pressure of the WO$_3$ films to 0.67 Pa (Fig. 1(a)). A lower deposition pressure during
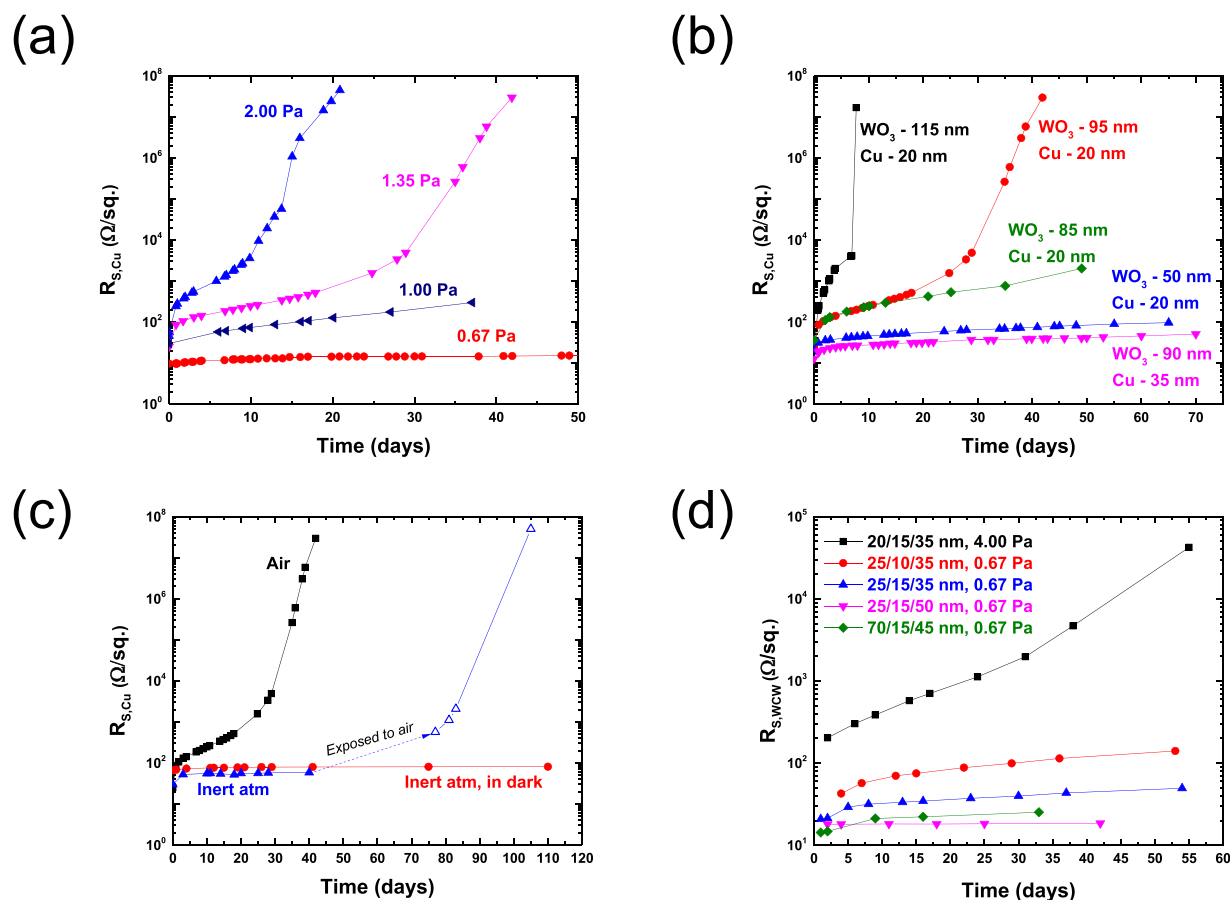
Fig. 1. Evolution of sheet resistance of inner Cu film ($R_{S,Cu}$) in $WO_3/Cu/WO_3$ coatings over time as a function of (a) deposition pressure of both WO_3 films (samples 1, 2, 7 and 12), (b) thickness (samples 4, 5, 7, 8 and 9) and (c) storage conditions (sample 6). (d) Evolution of sheet resistance of $WO_3/Cu/WO_3$ surface ($R_{S,WCW}$) as a function of the thickness and deposition pressure of both WO_3 films (samples 13–17).

magnetron sputtering generally results in denser films that inhibit Cu migration into them. Magnetron sputtering is a more energetic deposition technique compared to evaporation. It ensures a more uniform coverage due to the higher adatom mobility on the surface of the growing film and thus higher electrical conductivity of ultrathin films due to the continuing percolation path. The thickness of the $WO_3/Cu/WO_3$ coatings also influences their stability. As can be seen in Fig. 1(b), thinner WO_3 or thicker Cu films improve the stability.

To investigate the effect of ambient conditions on the evolution of $R_{S,Cu}$, two twin samples of sample 6 (Table 1) were placed in an Ar-containing glovebox. One of them was kept in the dark to prevent possible photocatalytic processes in the WO_3 films. Samples that would otherwise be unstable in air were found to be stable in an inert atmosphere (Fig. 1(c)). The difference in $R_{S,Cu}$ between the samples stored in the glovebox was small and within the error range of this study. Therefore, we conclude that the exposure of the coatings to daylight is not responsible for the sample degradation. When one of them was removed from the glovebox, the increase in resistance was initiated. The sample became insulating within ~60 d of exposure to air, while the twin sample kept in the glovebox maintained high conductivity (Fig. 1(c)). This indicates that the oxidation of Cu is the main reason for the decrease in conductivity rather than its migration only.

The high susceptibility of Cu to oxidation in air is well known. The oxidation kinetics of Cu films depend on several factors, including their microstructure and thickness. The thickness of the native oxide on the surface of a polycrystalline Cu film ranged from ~3.5 to ~6.0 nm after 100 d of oxidation in air [33]. Point defects, such as oxygen vacancies and interstitials, can facilitate the diffusion of oxygen into oxides [34]. Considering that the gradual penetration of oxygen and water into

electronic devices is inevitable even with encapsulation [35,36], there was a strong possibility that oxygen could pass through the upper WO_3 film to oxidize the Cu film. It can be seen in Fig. 1(b) that the stability of the coating was improved by increasing the thickness of the inner Cu film. In contrast, the samples were less stable for an unknown reason when the thickness of both WO_3 films was increased, indicating that additional mechanisms were involved.

To achieve low surface resistance ($R_{S,WCW}$), the second set of samples was produced by decreasing the thickness of both WO_3 films and keeping the thickness of the Cu film in the range of 10 to 15 nm (see second set of samples in Table 1). The thickness of the $WO_3/Cu/WO_3$ structure was modeled by CompleteEASE software to achieve the highest possible light transmittance at 550 nm. The optical constants of WO_3 and Cu used in the model were taken from SE measurements of the pure Cu film and the bottom WO_3 film of sample 8 (see Section 3.5 below). The modeling suggested a structure of 70/15/45 nm. The transmittance and specular reflectance spectra of the second set of samples are shown in Fig. 2. Indeed, the thickness structure proposed by the model (sample 16) provided the highest optical transmittance of 65% at 600 nm due to the suppressed reflectance. The performance of the deposited $WO_3/Cu/WO_3$ films was estimated using the figure-of-merit of Haacke ($T^{10}/R_{S,WCW}$) [4]. Sample 6 exhibits a figure-of-merit of 5×10^{-4} Ω^{-1}. Fig. 1(d) shows the evolution of $R_{S,WCW}$ for the second set of samples. The $R_{S,WCW}$ measured immediately after deposition ranged from ~14 to ~200 Ω/sq., again depending on the deposition parameters and the thickness of the samples. Higher deposition pressure during the WO_3 film growth (4.00 Pa in this case) or a thinner Cu film (10 nm) were observed to result in less stable coatings with higher $R_{S,WCW}$, similar to the first set of samples.
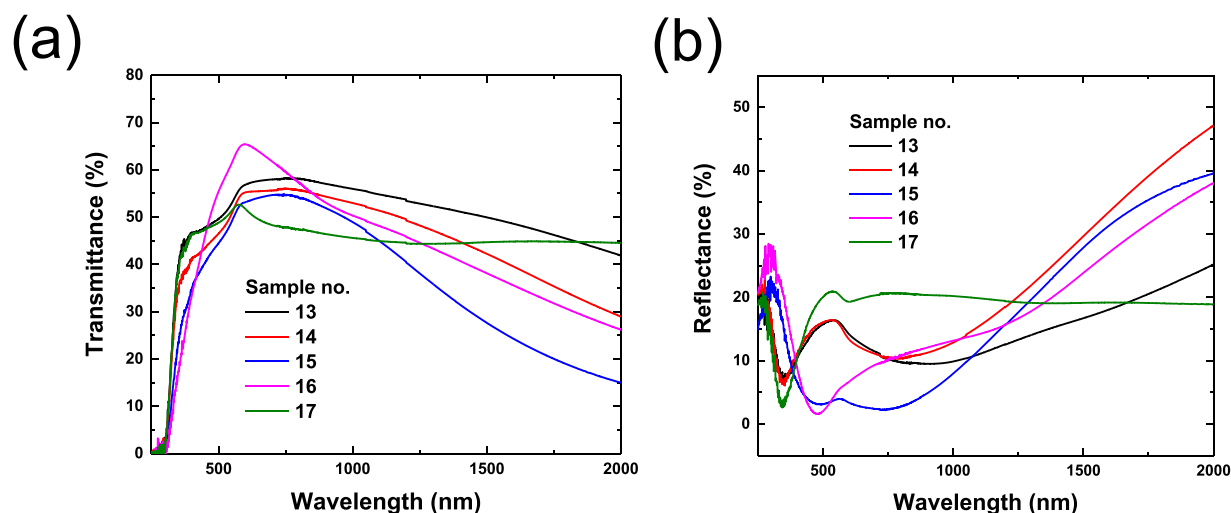
Fig. 2. (a) Transmittance and (b) specular reflectance of $WO_3/Cu/WO_3$ coatings on soda-lime glass substrates in the range of 250–2000 nm.

3.2. XPS measurements

XPS measurements, including depth profiling of the composition, were performed with the intention of confirming the migration of Cu and determining the chemical states of Cu and W. Fig. 3(a) and 3(b) show the depth profiles for sample 6, which was exposed to air, and its twin sample, which was stored in an Ar atmosphere, respectively. The XPS analysis shows the presence of W, O and Cu signals in the coatings and the three-layer structure is clearly distinguishable. In both cases, the presence of Cu (~1 at.%) in the upper WO_3 films was observed. As can be seen, Cu migration in WO_3 films occurs regardless of the storage conditions and was not responsible for the increase in the sheet resistance $R_{S,Cu}$ of the inner Cu film. In addition, on the surface, Cu accumulates up to ~25 at.% for the sample exposed to air and only up to ~2 at.% for the sample stored in Ar. Although this difference is significant, the values are approximate because they vary depending on the location of a measurement spot on the sample.

High-resolution spectra of the Cu 2p transitions are shown in Fig. 3 (c) and (d). The Cu 2p chemical state on the surface differs between the two samples. The Cu $2p_{3/2}$ peak in Fig. 3(c) contains at least two sub-peaks with binding energies (BEs) of 933.0 and 934.7 eV, which correspond to cupric oxide (CuO) [37] and another Cu^{2+} containing compound or mixture of compounds, for example, $Cu(OH)_2$ [38] or $CuCO_3$ [39,40], respectively. The strong satellite feature centered at ~943 eV is additional strong evidence that supports the presence of predominantly divalent copper in the very outer layer [37]. The Cu 2p spectra measured for the sample stored in an Ar atmosphere (Fig. 3(d)) reveal a narrow peak centered at 932.6 eV, which could be attributed to cuprous oxide (Cu_2O) or metallic Cu^0 [37]. The shape of the Auger spectrum (inset of Fig. 3(d)) measured for the $L_4M_{4,5}M_{4,5}$ transition and the value of the modified Auger parameter (~1848.4 eV) suggest that the copper-containing compound present at the very surface of the sample is Cu_2O. The presence of a very weak satellite feature at 947 eV indicates the vanishingly small content of divalent Cu compounds in the sample. Since copper-containing compounds are prone to reduction during Ar-ion etching, it was not possible to reliably determine the chemical state of Cu deeper in the coating.

The BEs of the peaks corresponding to W $4f_{7/2}$ and W $4f_{5/2}$ for both samples were determined at 36.2 and 38.3 eV, respectively (Fig. 3(e) and 3(f)). The additional peak centered at 42.1 eV is ascribed as a loss feature of W. The positions of the peaks correspond to W with the oxidation state of 6+ (WO_3) [25,41]. Detailed data of Cu 2p and W 4f peaks detected from the surface of sample 6 can be found in Table S1. Based on the measured intensities, the chemical composition of the upper tungsten oxide film for the sample stored in Ar is close to

stoichiometric WO_3 (W 24 at.% and O 74 at.%).

3.3. X-ray diffraction measurements

X-ray diffraction measurements of the samples show only one low-intensity peak at $2\theta = 43.3°$, which originates from the metallic Cu film between the dielectric WO_3 films, which are X-ray amorphous. The evolution of this Cu (111) peak for sample 9 was studied over a longer period of time (Fig. 4). The peaks were fitted with the Voigt function to remove noise and accurately determine the peak parameters. The intensity of the peak decreases with time together with increasing resistance of the inner Cu film (Fig. 4(b)). This is a clear result of the oxidation and Cu migration into the WO_3 films. Other peak parameters, such as position and full width at half maximum (FWHM), did not show a clear correlation with the sheet resistance $R_{S,Cu}$ or time. On average, the FWHM value is 1°, which corresponds to a Cu crystallite size of approximately 10 nm according to the Scherrer equation.

3.4. SEM and TEM measurements

The surface morphology and cross-sectional images of the $WO_3/Cu/WO_3$ samples obtained by electron microscopy are shown in Fig. 5. A dense surface microstructure was confirmed by SEM of the upper WO_3 films, as shown in Fig. 5(a). The surface consists of randomly shaped nanosized grains with round edges and an average size of less than ~20 nm. The observed microstructure is as expected since the magnetron sputtering technique is known for producing dense coatings. The cross-sectional image in Fig. 5(b) clearly shows the distinct three-layer structure of $WO_3/Cu/WO_3$. No cracks or large voids were observed either on the surface or in the cross-sectional images. The high-resolution TEM image of the WO_3/Cu interface in Fig. 5(c) reveals randomly oriented crystallites with a size of ~5 nm in the WO_3 film. Due to the small size, XRD does not show the nanocrystalline nature. Raman spectroscopy also revealed the nanocrystalline WO_3 structure in a previous study [25].

3.5. SE analysis

First, the single-layer WO_3 samples were measured by SE. The data analysis revealed that the thickness non-uniformity estimation was sufficient by applying a depolarization measurement (Table 2). For small samples, such as 25 × 25 mm (Fig. S1), it is not necessary to measure the sample in different places. Most of the samples have thickness non-uniformity of ~10%. This is an acceptable value when the deposition is performed without movement of the substrate. No voids or
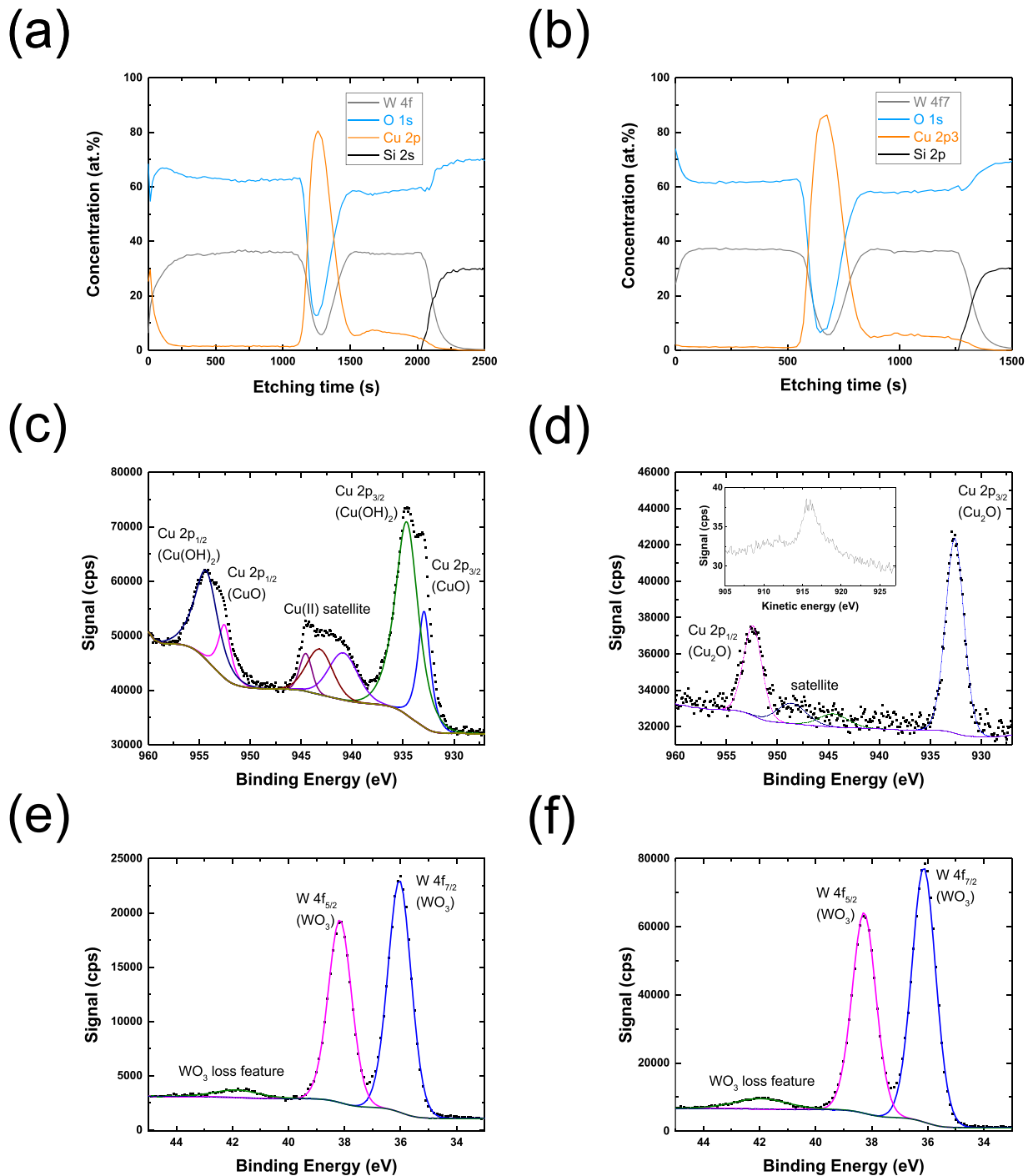
Fig. 3. XPS depth profiles and high-resolution X-ray photoelectron spectra of Cu 2p and W 4f for WO₃/Cu/WO₃ (90/20/90 nm) sample 6 (a, c, e) exposed to air and (b, d, f) stored in Ar.

strain-induced effects (e.g., optical gradient) are found within the single-layer WO₃ samples. The only inhomogeneities are the thickness non-uniformity and the small surface roughness of ∼4 nm. Refractive index n and extinction coefficient k dispersion curves as a function of photon energy E for single-layer WO₃ thin films are given in Fig. 6(a) and 6(b), respectively. The Tauc band gap is ∼3.2 eV, which is comparable with the data found in the literature. Stoichiometric WO₃ is transparent and insulating with a band gap of 3.0 to 3.3 eV [42,43], while the presence of O vacancies results in optical absorption (blue color due to gap narrowing) and electrical conductivity [44,45]. In addition, the electronic properties, in particular the band gap, are found to be

sensitive to the spatial arrangement of the W and O atoms [42,43]. The linear increase of refractive index with decrease of deposition pressure was observed (inset of Fig. 6(a)) which is clearly related to densification of the films at lower pressures.

The main ellipsometric angles Ψ and Δ of the three-layer WO₃/Cu/WO₃ coatings are shown in Fig. 7 for samples 6 and 9. Changes in optical properties over time are clearly visible. They are more pronounced for the unstable sample 6 and less pronounced for the much more stable sample 9. The Ψ and Δ spectra of other samples produced in this study can be found in Table S2. The amplitudes of Ψ change over the entire spectral range with time, indicating a change in effective n of the three-
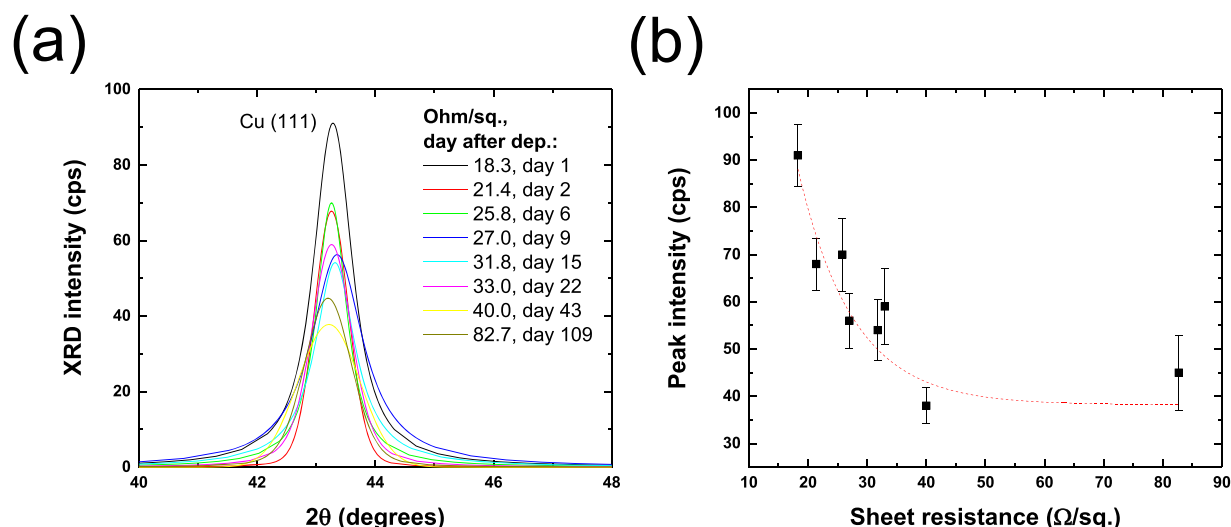
(a)

(b)

Fig. 4. (a) Evolution of X-ray diffraction (111) Cu peak for $WO_3/Cu/WO_3$ sample 9, and (b) its intensity as a function of sheet resistance $R_{S,Cu}$.
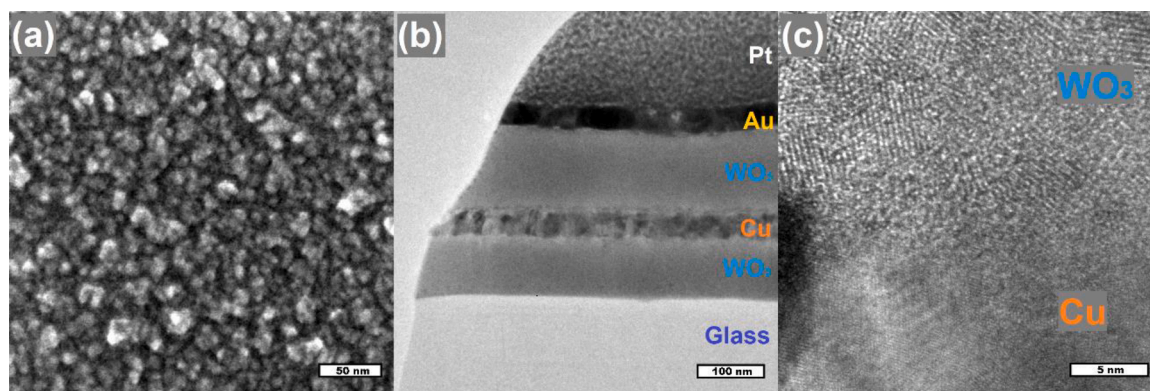

Fig. 5. (a) Surface SEM image of $WO_3/Cu/WO_3$ sample 16. (b) High-resolution TEM images of cross section (lamella) of (b) three-layer structure (sample 10) and (c) the interface between Cu and WO_3 films for sample 6.

Table 2
Thickness values (d_1, d_2 and d_3) of single-layer WO_3 thin films measured by SE at three different places, mean values and standard deviation for (d_1, d_2 and d_3), thickness non-uniformity obtained from d measurements at three different places compared to values obtained from single depolarization measurement by SE, as well as Tauc band gap E_g (obtained directly from the TLO oscillator) and refractive index value at 632.8 nm.

Sample	Thickness d excluding roughness (~4 nm), nm			Mean ± St. Dev. + Error	Thickness non-uniformity (%)		E_g, eV	n@632.8, nm
	d_1	d_2	d_3		3 spots	Depol.		
1	93.37	98.23	88.17	93.3 ± 5.1	5	12	3.23	2.16
2	73.13	79.29	66.57	73.0 ± 6.4	9	8	3.18	2.14
3	91.02	82.01	99.45	90.8 ± 8.8	10	8	3.20	2.11
4	53.68	62.59	47.21	54.5 ± 7.9	15	–	3.22	2.11
6	89.12	81.65	95.60	88.8 ± 7.1	8	11	3.24	2.09
8	113.62	104.03	124.87	114.2 ± 10.6	9	9	3.22	2.10
9	88.08	77.64	99.59	88.4 ± 11.2	13	11	3.24	2.11
10	113.43	104.76	125.16	114.5 ± 10.3	9	9	3.25	2.09
11	87.15	81.23	95.87	88.1 ± 7.4	8	10	3.22	2.10
12	86.60	93.94	78.59	86.4 ± 7.8	9	7	3.26	2.08

layer structures. The peak at ~1.3–1.7 eV is mainly affected by the middle Cu film. The decrease in amplitude of this peak indicates that the thickness of the metallic Cu film and/or the Cu EMA volume fraction is decreasing. This can be seen in most samples measured after one month. The reason for this can be both Cu migration in the WO_3 films and/or its oxidation. The peak positions in the Ψ and Δ spectra are almost unchanged (Fig. 7 and Table S2), indicating that the total thickness of the three-layer coatings remains the same when comparing the spectra of newly deposited samples and after one month. The small variation in

peak positions could be related with the thickness non-uniformity measured by depolarization, as summarized in Table 2. It is very likely that when re-measuring the sample after a month, the measurement spot on the sample was slightly different from the first measurement immediately after deposition. In contrast, the thickness of each film is expected to be slightly different due to the Cu migration and oxidation processes after one month. For most samples, the CuO EMA volume fraction increased and the Cu EMA volume fraction decreased over time. It was not sufficient to keep EMA volume fraction as the only
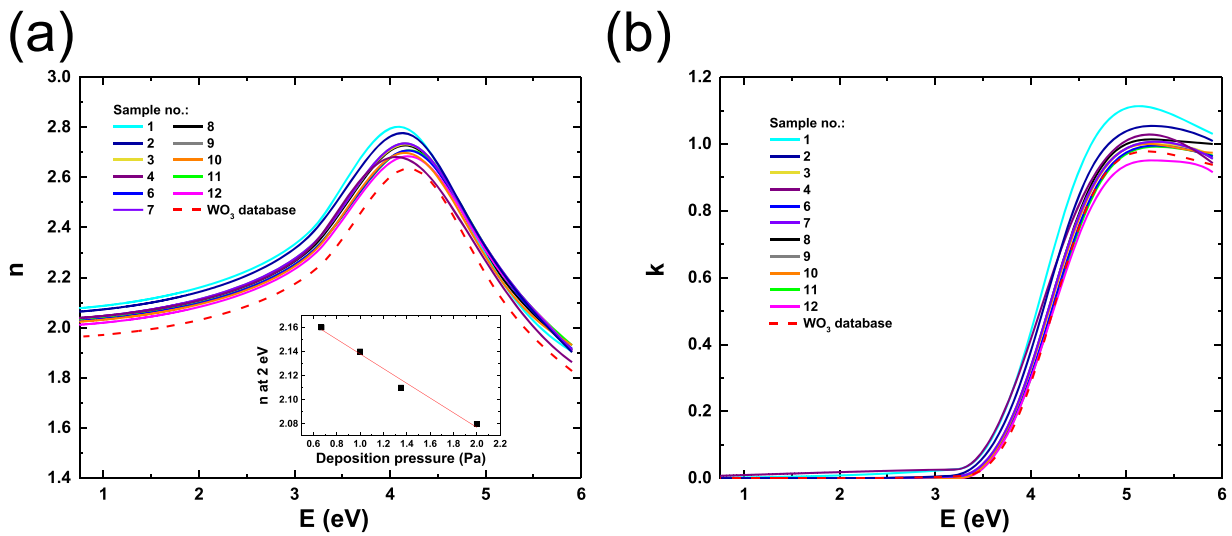
Fig. 6. (a) Refractive index *n* and (b) extinction coefficient *k* dispersion curves as a function of photon energy *E* for single-layer WO$_3$ thin films. The inset in (a) shows *n* at 2 eV as a function of deposition pressure.
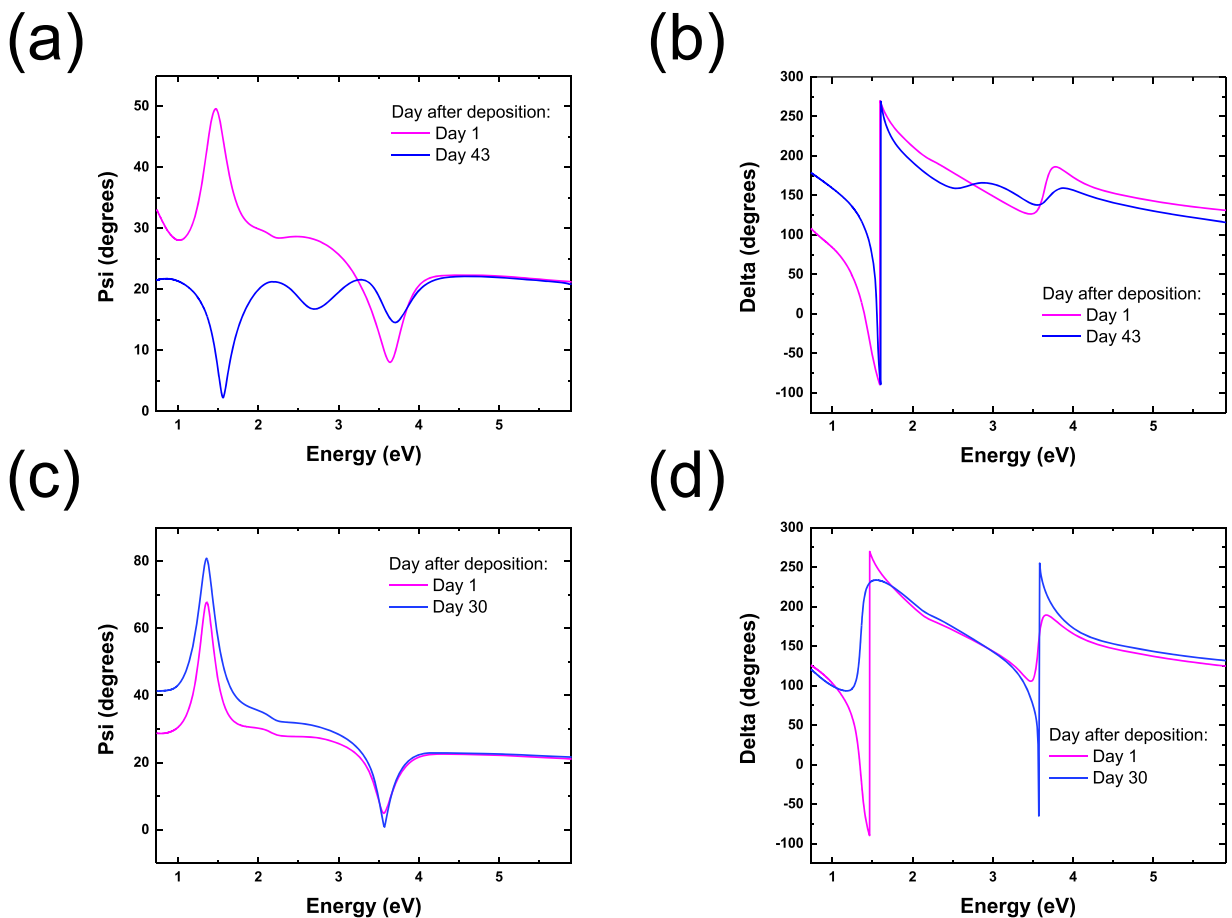

Fig. 7. Ψ and Δ spectra of samples (a, b) 6 and (c, d) 9 at an incident angle of 55° measured immediately after deposition and after 43 or 30 d, respectively.

fitting parameter in the model. To compensate for this variation, it was necessary to also vary the thickness of all three films; however, the total thickness variation was still within the range of thickness non-uniformity values.

From the SE measurements, only samples 9 and 10 show relatively small variations in the spectra over time, indicating that these two samples experience little change in optical properties when comparing the newly deposited samples and the samples measured after one month. The samples also showed only a slight increase in $R_{S,Cu}$ over time (Fig. 1 (b)). The main difference between these and other samples is the higher Cu thickness value of 35 and 50 nm, respectively (Table 1).

During the modeling of the EMA depth profile, the fitting parameters of the newly deposited samples were thickness, roughness, thickness non-uniformity and the EMA volume fraction of voids, CuO and Cu in

the WO$_3$ films. For the re-measured samples (after one month), some fitting parameters were kept constant (EMA volume fraction of voids, roughness and thickness non-uniformity), since it would be rather difficult for these values to change over time. The lowest mean square error (MSE) values were found for the depth profile EMA models, as illustrated in Fig. S2(b). The best model fits showed that some samples contain a WO$_3$ and CuO mixture, while all samples have a WO$_3$ and void mixture and for the middle film, a Cu and WO$_3$ mixture. The MSE of the model increased when the middle film was considered as a mixture of Cu and CuO. The MSE error also increased when the WO$_3$ films were considered as a mixture of void and Cu. The depth profile in each film arrives from the variation of the EMA volume fraction of voids and/or CuO within the WO$_3$ films and with the variation of Cu EMA volume fraction in the middle film of Cu.

The depth profiles of refractive index n and extinction coefficient k at 1.96 eV for samples 1 and 2 are presented in Fig. 7. The depth profiles of the remaining samples can be found in Table S3. Depending on the sample, the n values of both WO$_3$ films varied widely from ~1.7 to ~2.3 at 1.96 eV and exhibit a more or less pronounced gradient perpendicular to the substrate surface. This is due to the migration of Cu and/or the consequent presence of CuO in the WO$_3$ films. The k values of the WO$_3$ films are in most cases close to zero with a slight tendency to increase after one month (Table S3). In the middle Cu film for the newly deposited coatings, n at 1.96 eV decreases and also vary significantly from sample to sample in the range of ~0.4–1.5. After one month, there

is a strong tendency for n to increase. In the less stable coatings, values as high as 2.2 could be found. In the Cu films, k values are of 2–3, while after a month, they decrease to ~1–2. The exception is sample 1, for which WO$_3$ films were deposited at a lower pressure of 0.67 Pa.

In summary, samples 1 (Fig. 8](a) and (b)), 4, 9 and 10 have much smaller changes in optical properties over time in respect to other samples. The change after one month mainly appears only in the Cu film. The optical properties of the WO$_3$ films essentially do not change. These samples again appear more stable in accordance with the evolution of $R_{S,Cu}$, as summarized in Fig. 1. Sample 2 is an example of an unstable sample for which n and k in the average Cu film change significantly after a month (Fig. 8(c) and (d)).

There is reasonable agreement between the nominal thicknesses of each film and those obtained by SE (Table 1). The exceptions are samples 3, 10 and 12, where the estimated thicknesses for the first and second films do not match the nominal thickness, even considering the non-uniformity of the thickness. In contrast, the total thickness of the coatings obtained by SE is in good agreement with the nominal value, again considering the thickness non-uniformity.

3.6. Antimicrobial activity

The CFU log reduction and reduction in percentage after 2 h of incubation on the test sample surfaces of both *E. coli* and *S. aureus* bacterial culture suspensions is visualized in Fig. 9(a,b). The *E. coli* log reduction
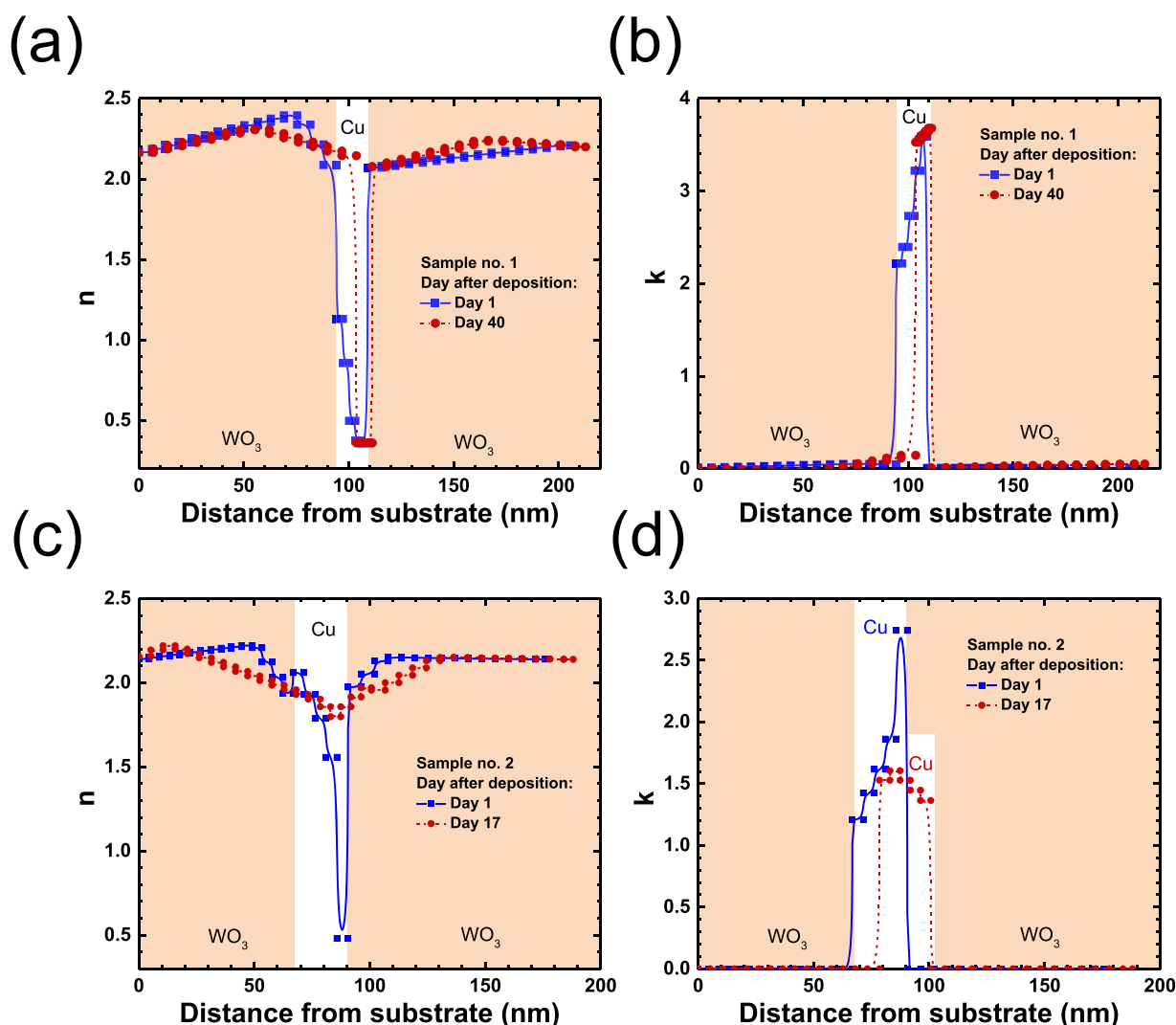

Fig. 8. n and k depth profiles (at 1.96 eV) of WO$_3$/Cu/WO$_3$ samples (a, b) 1 and (c, d) 2.
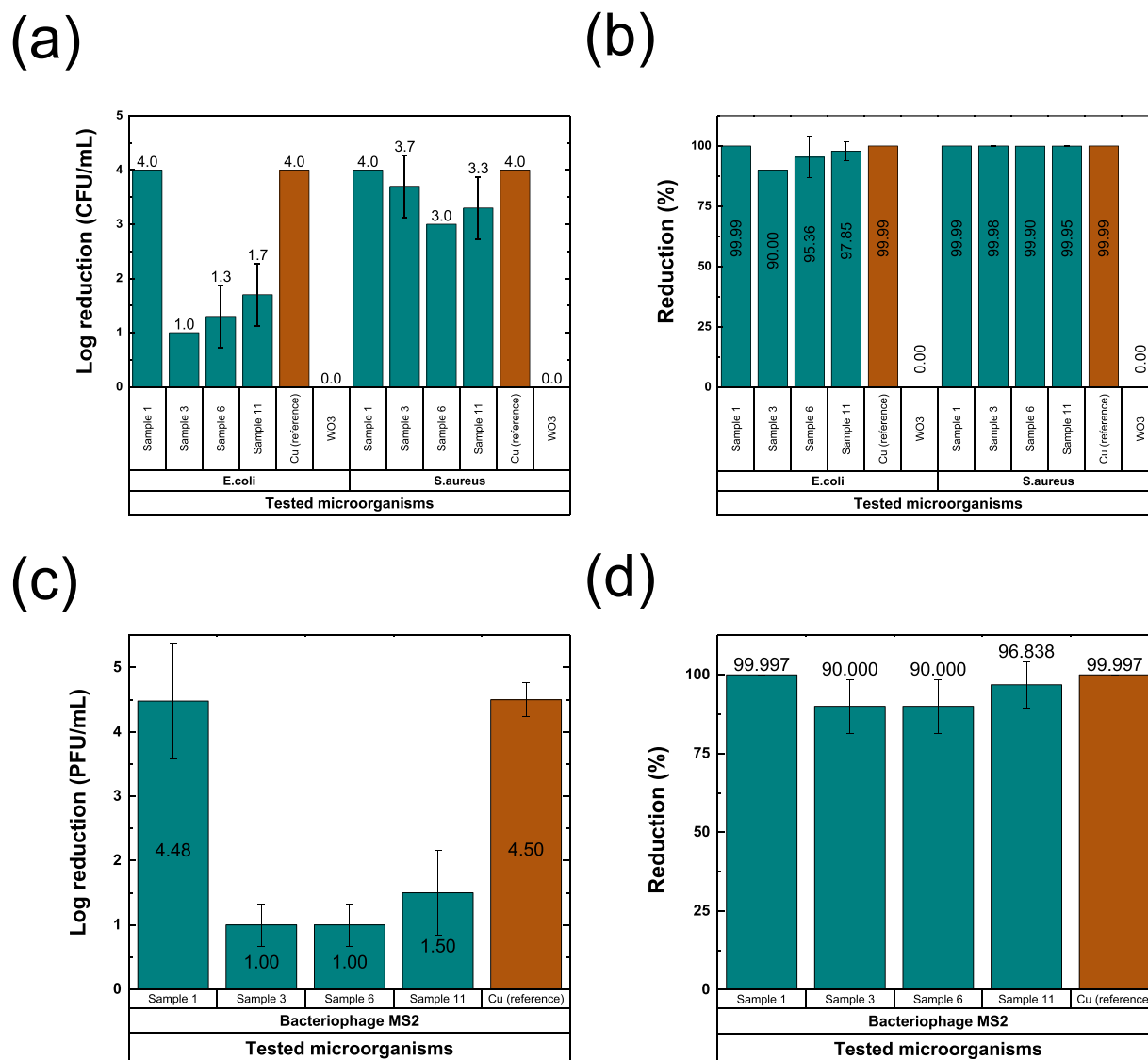
Fig. 9. Antimicrobial tests of samples 1, 3, 6 and 11, pure Cu (reference) and pure WO₃. (a) CFU log reduction and (b) reduction in percentage of *E. coli* and *S. aureus* compared to a pure PET substrate. (c) PFU log reduction and (d) reduction in percentage of MS2 bacteriophage compared to a pure PET substrate. Error bars represent the standard deviation between three separate iterations.

rate of 4 was achieved by the application of sample 1 and the pure copper (reference) film. Samples 3, 6 and 11 with oxygen flow rates of 15, 20 and 25 sccm, respectively, and the sputtering pressure of 1.35 Pa during the WO₃ film deposition were less effective against *E. coli* with the log reduction rates between 1.0 and 1.7. The *S. aureus* bacteria were generally more vulnerable under the same test conditions compared to *E. coli.* The *S. aureus* CFU log reduction rates after the contact with sample 1 and the reference (Cu sample) were above 4 and exceeded the measurement range of the testing methodology showing complete inactivation or destruction of bacterial cells. The log reduction rates of 3.6, 3.0 and 3.3 for samples 3, 6 and 11, respectively, were smaller. The pure WO₃ coatings showed no antimicrobial activity against both bacterial cultures, indicating the key role of Cu in killing bacteria. Nevertheless, other authors have reported that tungsten oxide may possess the growth inhibition properties against *S. aureus* and bacteriophage T4, which is likely due to a photo-killing mechanism [46].

The results of the tests with MS2 bacteriophage are presented in Fig. 9(c,d). The application of sample 1 and the pure copper (reference) film causes a PFU log reduction rate of 4.5 in both cases. In contrast, the log reduction rates for samples 3, 6 and 11 are only in the range from 1 to 1.5. A lower sputtering pressure is, therefore, advantageous because

the samples are not only more stable but also have higher antimicrobial properties.

Samples 14 and 17 from the second set with the optimized optical and electrical properties (higher figure of merit) were tested only by *E. coli* gram-negative bacteria due to the higher level of culture durability against the samples. In addition, the concentration of the initial bacterial suspension was lowered to 1 × 10⁵ CFU/mL to indemnify test selectivity. Under these conditions, the tests were also carried out with sample 1 and the pure Cu reference (Fig. 10) to properly compare the samples from the second set, with the best sample from the first set. Sample 1 showed a log reduction rate of 1.75 under the new testing conditions. In contrast, sample 14 with the higher figure-of-merit also exhibits a larger log reduction of >2.8. Again, by increasing the sputtering pressure during WO₃ growth (sample 17), the log reduction decreases down to 1.39.

4. Conclusions

The oxidation and migration of Cu in WO₃ films over time causes changes in the physical properties of three-layer WO₃/Cu/WO₃ coatings. This instability can be reduced by using denser coatings, usually
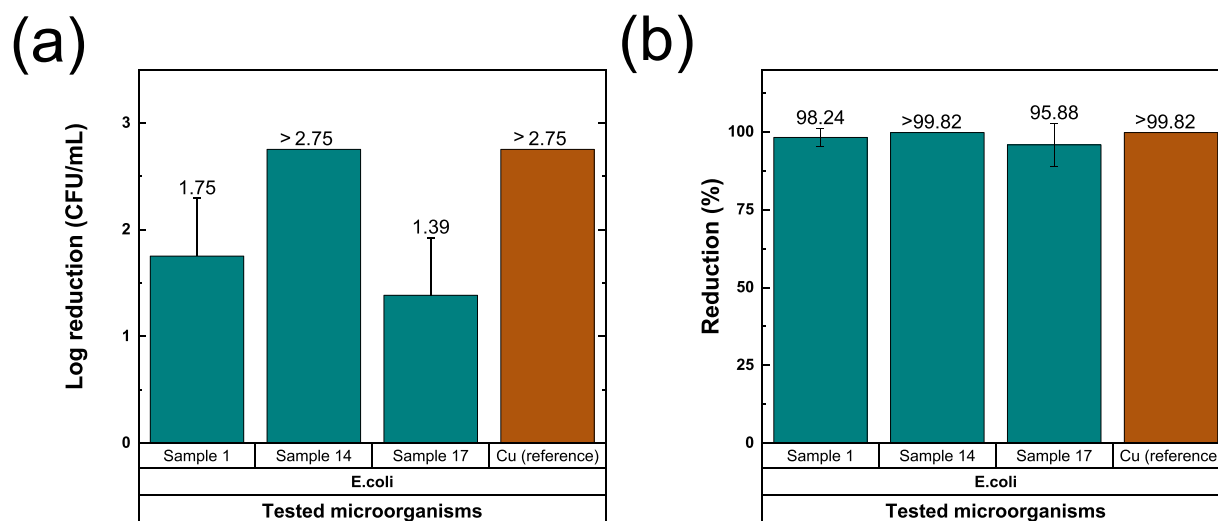
10

Fig. 10. (a) CFU log reduction and (b) reduction in percentage of *E. coli* compared to a pure PET substrate for samples 1, 14 and 17 and pure Cu (reference). Error bars represent the standard deviation between three separate iterations.

obtained at lower pressures by magnetron sputtering, to protect the thin inner Cu film from environmental influences. The thickness structure also strongly affects the stability of the coatings, as well as the optical and electrical properties. The main reason for the decrease in electrical conductivity is the oxidation of Cu. The coatings show decent antimicrobial activity against *E. coli* and *S. aureus* bacteria, as well as the MS2 (*Emesvirus zinderi*) bacteriophage virus. In the framework of this study, it was observed that more stable samples also showed higher antimicrobial activity. The multifunctionality consisting of transparent conductive properties and antimicrobial activity can be effectively used where it is needed as a single three-layer coating.

CRediT authorship contribution statement

M. Zubkins: Writing – original draft, Visualization, Supervision, Methodology, Investigation, Formal analysis, Data curation, Conceptualization. **V. Vibornijs:** Formal analysis, Methodology, Investigation, Writing – original draft, Conceptualization. **E. Strods:** Methodology, Investigation. **I. Aulika:** Writing – original draft, Visualization, Methodology, Investigation, Funding acquisition, Formal analysis, Data curation. **A. Zajakina:** Supervision, Methodology, Resources, Project administration, Funding acquisition. **A. Sarakovskis:** Writing – original draft, Visualization, Investigation, Formal analysis. **K. Kundzins:** Visualization, Investigation, Formal analysis. **K. Korotkaja:** Investigation, Formal analysis. **Z. Rudevica:** Investigation. **E. Letko:** Investigation. **J. Purans:** Supervision, Conceptualization, Resources, Project administration, Funding acquisition.

Declaration of Competing Interest

The authors declare the following financial interests/personal relationships which may be considered as potential competing interests:

Martins Zubkins reports financial support was provided by European Regional Development Fund. Viktors Vibornijs reports financial support was provided by European Regional Development Fund. Edvards Strods reports financial support was provided by European Regional Development Fund. Ilze Aulika reports financial support was provided by European Regional Development Fund. Anna Zajakina reports financial support was provided by European Regional Development Fund. Karlis Kundzins reports financial support was provided by European Regional Development Fund. Ksenija Korotkaja reports financial support was provided by European Regional Development Fund. Viktors Vibornijs has patent #EP23158463.2 pending to Institute of Solid State Physics,

University of Latvia. Viktors Vibornijs has patent #LVP2020000079 issued to Institute of Solid State Physics, University of Latvia. Martins Zubkins has patent #EP23158463.2 pending to Institute of Solid State Physics, University of Latvia. Martins Zubkins has patent #LVP2020000079 issued to Institute of Solid State Physics, University of Latvia. Juris Purans has patent #EP23158463.2 pending to Institute of Solid State Physics, University of Latvia. Juris Purans has patent #LVP2020000079 issued to Institute of Solid State Physics, University of Latvia. Edvards Strods has patent #EP23158463.2 pending to Institute of Solid State Physics, University of Latvia. Ilze Aulika has patent #EP23158463.2 pending to Institute of Solid State Physics, University of Latvia. Anna Zajakina has patent #EP23158463.2 pending to Institute of Solid State Physics, University of Latvia. Anna Zajakina has patent #LVP2020000079 issued to Institute of Solid State Physics, University of Latvia. Ksenija Korotkaja has patent #EP23158463.2 pending to Institute of Solid State Physics, University of Latvia. Zanna Rudevica has patent #EP23158463.2 pending to Institute of Solid State Physics, University of Latvia.

Data availability

Data will be made available on request.

Acknowledgments

References

[1] C. Ji, D. Liu, C. Zhang, L.J. Guo, Ultrathin-metal-film-based transparent electrodes with relative transmittance surpassing 100%, Nat. Commun. 11 (2020) 1–8, https://doi.org/10.1038/s41467-020-17107-6.

[2] O. Inganäs, Avoiding indium, Nat. Photon 5 (2011) 201–202, https://doi.org/10.1038/nphoton.2011.46.

[3] G. Torrisi, I. Crupi, S. Mirabella, A. Terrasi, Robustness and electrical reliability of AZO/Ag/AZO thin film after bending stress, Sol. Energy Mater. Sol. Cells 165 (2017) 88–93, https://doi.org/10.1016/j.solmat.2017.02.037.

[4] G. Haacke, New figure of merit for transparent conductors, J. Appl. Phys. 47 (1976) 4086–4089, https://doi.org/10.1063/1.323240.

[5] L. Cattin, El. Jouad, N. Stephant, G. Louarn, M. Morsli, M. Hssein, Y. Mouchaal, S. Thouiri, M. Addou, A. Khelil, Dielectric/metal/dielectric alternative transparent electrode: observations on stability/degradation, J. Phys. D: Appl. Phys. 50 (2017), 375502, https://doi.org/10.1088/1361-6463/aa7dfd.

[6] B. Lin, C. Lan, C. Li, Z. Chen, Effect of thermal annealing on the performance of WO$_3$-Ag-WO$_3$ transparent conductive film, Thin Solid Films 571 (2014) 134–138, https://doi.org/10.1016/j.tsf.2014.10.045.

[7] S.M. Imani, L. Ladouceur, T. Marshall, R. Maclachlan, L. Soleymani, T.F. Didar, Antimicrobial nanomaterials and coatings: current mechanisms and future perspectives to control the spread of viruses including SARS-CoV-2, ACS Nano 14 (2020) 12341–12369, https://doi.org/10.1021/acsnano.0c05937.

[8] L. Cobrado, A. Silva-Dias, M.M. Azevedo, A.G. Rodrigues, High-touch surfaces: microbial neighbours at hand, Eur. J. Clin. Microbiol. Infect. Dis. 36 (2017) 2053–2062, https://doi.org/10.1007/s10096-017-3042-4.

[9] H. Huang, C. Fan, M. Li, H.L. Nie, F.B. Wang, H. Wang, R. Wang, J. Xia, X. Zheng, X. Zuo, J. Huang, COVID-19: a call for physical scientists and engineers, ACS Nano 14 (2020) 3747–3754, https://doi.org/10.1021/acsnano.0c02618.

[10] C. Adlhart, J. Verran, N.F. Azevedo, H. Olmez, M.M. Keinänen-Toivola, I. Gouveia, L.F. Melo, F. Crijns, Surface modifications for antimicrobial effects in the healthcare setting: a critical overview, J. Hosp. Infect. 99 (2018) 239–249, https://doi.org/10.1016/j.jhin.2018.01.018.

[11] W. DeFlorio, S. Liu, A.R. White, T.M. Taylor, L. Cisneros-Zevallos, Y. Min, E. M. Scholar, Recent developments in antimicrobial and antifouling coatings to reduce or prevent contamination and cross-contamination of food contact surfaces by bacteria, Compr. Rev. Food Sci. Food Saf. 20 (2021) 3093–3134, https://doi.org/10.1111/1541-4337.12750.

[12] I.C. Lee, J.W. Ko, S.H. Park, J.O. Lim, I.S. Shin, C. Moon, S.H. Kim, J.D. Heo, J. C. Kim, Comparative toxicity and biodistribution of copper nanoparticles and cupric ions in rats, Int. J. Nanomed. 16 (2016) 2883–2900, https://doi.org/10.2147/IJN.S106346.

[13] Z. Ferdous, A. Nemmar, Health impact of silver nanoparticles: a review of the biodistribution and toxicity following various routes of exposure, Int. J. Mol. Sci. 21 (2020) 2375, https://doi.org/10.3390/ijms21072375.

[14] M. Rosenberg, K. Ilić, K. Juganson, A. Ivask, M. Ahonen, I.V. Vrček, A. Kahru, Potential ecotoxicological effects of antimicrobial surface coatings: a literature survey backed up by analysis of market reports, PeerJ 7 (2019) e6315, https://doi.org/10.7717/peerj.6315.

[15] G. Duan, L. Chen, Z. Jing, P.D. Luna, L. Wen, L. Zhang, L. Zhao, J. Xu, Z. Li, Z. Yang, R. Zhou, Robust antibacterial activity of tungsten oxide (WO$_{3-x}$) nanodots, Chem. Res. Toxicol. 32 (2019) 1357–1366, https://doi.org/10.1021/acs.chemrestox.8b00399.

[16] S. Cong, F. Geng, Z. Zhao, Tungsten oxide materials for optoelectronic applications, Adv. Mater. 28 (2016) 10518–10528, https://doi.org/10.1002/adma.201601109.

[17] R. Abe, H. Takami, N. Murakami, B. Ohtani, Pristine simple oxides as visible light driven photocatalysts: highly efficient decomposition of organic compounds over platinum-loaded tungsten oxide, J. Am. Chem. Soc. 130 (2008) 7780–7781, https://doi.org/10.1021/ja800835q.

[18] P. Zhou, Q. Xu, H. Li, Y. Wang, B. Yan, Y. Zhou, J. Chen, J. Zhang, K. Wang, Fabrication of two-dimensional lateral heterostructures of WS$_2$/WO$_3$· H$_2$O through selective oxidation of monolayer WS2, Angew. Chem. 127 (2015) 15441–15445, https://doi.org/10.1002/ange.201508216.

[19] H. Irie, S. Miura, K. Kamiya, K. Hashimoto, Efficient visible light-sensitive photocatalysts: grafting Cu (II) ions onto TiO$_2$ and WO$_3$ photocatalysts, Chem. Phys. Lett. 457 (2008) 202–205, https://doi.org/10.1016/j.cplett.2008.04.006.

[20] Y. Yao, K. Yamauchi, G. Yamauchi, T. Ochiai, T. Murakami, Y. Kubota, Synergistic antibacterial performance of a Cu/WO$_3$-added PTFE particulate superhydrophobic composite under visible-light exposure, J. Biomater. Nanobiotechnol. 3 (2012) 421, https://doi.org/10.4236/jbnb.2012.34042.

[21] B.M. Alshabander, Copper (II)-doped WO$_3$ nanoparticles with visible light photocatalytic antibacterial activity against gram-positive and gram-negative bacteria, Inorg. Nano-Met. Chem. 50 (2020) 1329–1333, https://doi.org/10.1080/24701556.2020.1749075.

[22] C.G. Granqvist, Transparent conductors as solar energy materials: a panoramic review, Sol. Energy Mater. Sol. Cells 91 (2007) 1529–1598, https://doi.org/10.1016/j.solmat.2007.04.031.

[23] K. Hong, K. Kim, S. Kim, I. Lee, H. Cho, S. Yoo, H.W. Choi, N.Y. Lee, Y.H. Tak, J. L. Lee, Optical properties of WO$_3$/Ag/WO$_3$ multilayer as transparent cathode in top-emitting organic light emitting diodes, J. Phys. Chem. C 115 (2011) 3453–3459, https://doi.org/10.1021/jp109943b.

[24] K.S. Yook, S.O. Jeon, C.W. Joo, J.Y. Lee, Transparent organic light emitting diodes using a multilayer oxide as a low resistance transparent cathode, Appl. Phys. Lett. 93 (2008), 013301, https://doi.org/10.1063/1.2955528.

[25] A. Šutka, M. Zubkins, A. Linarts, L. Lapčinskis, K. Ma¯lnieks, O. Verners, A. Sarakovskis, R. Grzibovskis, J. Gabrusenoks, E. Strods, K. Smits, V. Vibornijs, L. Bikse, J. Purans, Tribovoltaic device based on the W/WO$_3$ schottky junction operating through hot carrier extraction, J. Phys. Chem. C 125 (2021) 14212–14220, https://doi.org/10.1021/acs.jpcc.1c04312.

[26] A.S. Ferlauto, G.M. Ferreira, J.M. Pearce, C.R. Wronski, R.W. Collins, X. Deng, G. Ganguly, Analytical model for the optical functions of amorphous semiconductors from the near-infrared to ultraviolet: applications in thin film photovoltaics, J. Appl. Phys. 92 (2002) 2424–2436, https://doi.org/10.1063/1.1497462.

[27] D.E. Aspnes, J. Theeten, F. Hottier, Investigation of effective-medium models of microscopic surface roughness by spectroscopic ellipsometry, Phys. Rev. B 20 (1979) 3292, https://doi.org/10.1103/PhysRevB.20.3292.

[28] L.A. Pettersson, L. Hultman, H. Arwin, Porosity depth profiling of thin porous silicon layers by use of variable-angle spectroscopic ellipsometry: a porosity graded-layer model, Appl. Opt. 37 (1998) 4130–4136, https://doi.org/10.1364/AO.37.004130.

[29] I.P. López, L. Cattin, D.T. Nguyen, M. Morsli, J.C. Bernède, Dielectric/metal/dielectric structures using copper as metal and MoO$_3$ as dielectric for use as transparent electrode, Thin Solid Films 520 (2012) 6419–6423, https://doi.org/10.1016/j.tsf.2012.06.056.

[30] S. Tuo, L. Cattin, H. Essaidi, L. Peres, G. Louarn, Z. El Jouad, M. Hssein, S. Touihri, S. Yapi Abbe, P. Torchio, M. Addou, J.C. Bernède, Stabilisation of the electrical and optical properties of dielectric/Cu/dielectric structures through the use of efficient dielectric and of Cu: Ni alloy, J. Alloy. Compd. 729 (2017) 109–116, https://doi.org/10.1016/j.jallcom.2017.09.087.

[31] D.E. Rabia, M. Blais, H. Essaidi, N. Stephant, G. Louarn, M. Morsli, S. Touihri, J. C. Bernède, L. Cattin, Stabilisation of Cu films in WO$_3$/Ag/Cu: Al/WO$_3$ structures through their doping by Al and Ag, Thin Solid Films 669 (2019) 613–619, https://doi.org/10.1016/j.tsf.2018.11.059.

[32] L. Zhou, X. Chen, F. Zhu, X. Sun, Z. Sun, Improving temperature-stable AZO-Ag-AZO multilayer transparent electrodes using thin Al layer modification, J. Phys. D: Appl. Phys. 45 (2012), 505103, https://doi.org/10.1088/0022-3727/45/50/505103.

[33] J. Liu, H. Jiang, L. Zhang, H. Gu, X. Chen, S. Liu, Thickness dependent native oxidation kinetics observation and prediction for Cu films using spectroscopic ellipsometry, Appl. Surf. Sci. 518 (2020), 146236, https://doi.org/10.1016/j.apsusc.2020.146236.

[34] C. Kim, K.W. Park, D. Kalaev, C. Nicollet, H.L. Tuller, Effect of structure on oxygen diffusivity in layered oxides: a combined theoretical and experimental study, J. Mater. Chem. A 10 (2022) 15402–15414, https://doi.org/10.1039/D2TA02580A.

[35] G.D.M. Dabera, M. Walker, A.M. Sanchez, H.J. Pereira, R. Beanland, R.A. Hatton, Retarding oxidation of copper nanoparticles without electrical isolation and the size dependence of work function, Nat. Commun. 8 (2017) 1894, https://doi.org/10.1038/s41467-017-01735-6.

[36] S. Bhanushali, P. Ghosh, A. Ganesh, W. Cheng, 1D copper nanostructures: progress, challenges and opportunities, Small 11 (2015) 1232–1252, https://doi.org/10.1002/smll.201402295.

[37] M.C. Biesinger, Advanced analysis of copper X-ray photoelectron spectra, Surf. Interface Anal. 49 (2017) 1325–1334, https://doi.org/10.1002/sia.6239.

[38] J. Yu, J. Ran, Facile preparation and enhanced photocatalytic H$_2$-production activity of Cu (OH)$_2$ cluster modified TiO$_2$, Energy Environ. Sci. 4 (2011) 1364–1371, https://doi.org/10.1039/C0EE00729C.

[39] F. Liu, L. Csetenyi, G.M. Gadd, Amino acid secretion influences the size and composition of copper carbonate nanoparticles synthesized by ureolytic fungi, Appl. Microbiol. Biotechnol. 103 (2019) 7217–7230, https://doi.org/10.1007/s00253-019-09961-2.

[40] R.P. Vasquez, CuCO$_3$ by XPS, Surf. Sci. Spectra 5 (1998) 273–278, https://doi.org/10.1116/1.1247884.

[41] M.A. Arvizu, H.Y. Qu, U. Cindemir, Z. Qiu, E.A. Rojas-González, D. Primetzhofer, C.G. Granqvist, L. Österlund, G.A. Niklasson, Electrochromic WO$_3$ thin films attain unprecedented durability by potentiostatic pretreatment, J. Mater. Chem. A 7 (2019) 2908–2918, https://doi.org/10.1039/C8TA09621J.

[42] S.K. Deb, Optical and photoelectric properties and colour centres in thin films of tungsten oxide, Philos. Mag. 27 (1973) 801–822, https://doi.org/10.1080/14786437308227562.

[43] R. Vemuri, M. Engelhard, C. Ramana, Correlation between surface chemistry, density, and band gap in nanocrystalline WO$_3$ thin films, ACS Appl. Mater. Interfaces 4 (2012) 1371–1377, https://doi.org/10.1021/am2016409 (2012).

[44] J.F. Owen, K.J. Teegarden, H.R. Shanks, Optical properties of the sodium-tungsten bronzes and tugsten trioxide, Phys. Rev. B 18 (1978) 3827–3837, https://doi.org/10.1103/PhysRevB.18.3827.

[45] R.D. Bringans, H. Höchst, H.R. Shanks, Defect states in WO$_3$ studied with photoelectron spectroscopy, Phys. Rev. B 24 (1981) 3481–3489, https://doi.org/10.1103/PhysRevB.24.3481.

[46] R.K. Matharu, L. Ciric, G. Ren, M. Edirisinghe, Comparative study of the antimicrobial effects of tungsten nanoparticles and tungsten nanocomposite fibres on hospital acquired bacterial and viral pathogens, Nanomaterials 10 (2020) 1017, https://doi.org/10.3390/nano10061017.